Mechanical Engineering Advances 2025, 3(2), 2534.
https://doi.org/10.59400/mea2534

Article

Effect of inverse-square heat absorption on MHD natural convection flow in a vertical concentric annulus with radial and induced magnetic fields

Muhammad Yusuf Muhammad[1,*], Yusuf Ya'u Gambo[2], Muhammad Auwal Lawan[1]

[1] Department of Mathematics, Aliko Dangote University of Science and Technology, Kano 713103, Nigria
[2] Department of Mathematics, North West University, Kano 713103, Nigeria
*** Corresponding author:** Muhammad Yusuf Muhammad, muhammadyusufmuhammad@kustwudil.edu.ng

CITATION

Muhammad MY, Gambo YY, Lawan MA. Effect of inverse-square heat absorption on MHD natural convection flow in a vertical concentric annulus with radial and induced magnetic fields. Mechanical Engineering Advances. 2025; 3(2): 2534. https://doi.org/10.59400/mea2534

ARTICLE INFO

Received: 9 January 2025
Accepted: 17 February 2025
Available online: 3 April 2025

Abstract: This study investigates the impact of inverse-square heat absorption on steady, fully developed laminar MHD natural convection flow within an infinite vertical concentric annulus under the influence of applied radial and induced magnetic fields. The governing transport equations in the model were transformed into a non-dimensional form, allowing for the derivation of unified analytical solutions for the velocity, temperature, magnetic field, and induced current density distributions for both isothermal and iso-flux on the inner cylinder of concentric annuli. The influence of key physical parameters in the model is illustrated through a comprehensive analysis of graphs and tables. The findings reveal that increasing the heat absorption parameter intensifies thermal gradients near the inner cylinder, while stronger magnetic fields suppress fluid motion, reducing mass flux and enhancing flow resistance. Mass flux and induced current density decrease as Hartmann number and heat absorption parameter increase, demonstrating the combined influence of thermal and electromagnetic forces. The magnetic field distributions and associated current densities exhibit pronounced attenuation near the inner cylinder under a higher Hartmann number. These findings highlight the intricate interaction between thermal and electromagnetic forces, offering valuable insights for applications in nuclear reactors, MHD power generation, and advanced cooling technologies. This study contributes to refining MHD-driven thermal management approaches for Advanced engineering systems.

Keywords: MHD; natural convection; heat generation; vertical concentric annulus; Hartmann number; inverse-square heat generation

1. Introduction

The study of magnetohydrodynamic (MHD) natural convection in annular geometries is crucial for engineering applications such as power generation, nuclear cooling systems, and metallurgical processes. When a conducting fluid is exposed to an externally applied uniform magnetic field, an induced magnetic field is generated due to fluid motion and interaction with the applied field. The interaction between these fields affects heat transfer and flow stability, making it essential to distinguish their separate and combined influences.

There are numerous applications for studying natural convective flow along a vertical cylinder in fields like technology, agriculture, oceanography, and geothermal power generation. Applications in solar power collectors, magnetohydrodynamic power generator design, and oil thermal recovery have drawn attention to the study of transport phenomena with annular geometry.

The analysis and design of heat exchangers often rely on annular geometries due to their extensive applications in geophysics and engineering fields. These applications

include magnetohydrodynamic (MHD) power generation, geothermal energy systems, treatment of nuclear fuel debris, and solidification of metals and alloys. Notably, natural convective flows along vertical cylinders have found uses in solar power collection, geothermal energy extraction, and oil recovery. The integration of heat sources or sinks within a concentric annulus enhances fluid flow efficiency and overall system performance Kumar and Singh [1].

Magnetohydrodynamics, which bridges fluid mechanics and electromagnetism, facilitates the control and propulsion of electrically conducting fluids via Lorentz forces generated from interactions between magnetic fields and electric currents. In the context of vertical concentric annuli, studying MHD-natural convection interactions is critical for optimizing cooling systems in nuclear reactors, enhancing safety and operational efficiency [2]. Additionally, understanding the effects of radial and induced magnetic fields has practical implications for geothermal energy systems Kefayati and Ahmadi [3] and industrial processes such as MHD propulsion and metal solidification [4,5].

Heat generation and absorption significantly impact natural convection flows by altering temperature distributions and flow patterns. These effects are vital in various applications, including nuclear reactor cores, semiconductor manufacturing, and combustion modeling. Employing an inverse-square heat absorption model provides a realistic framework for simulating heat transfer in such systems, addressing a gap in the literature where most studies have focused on constant or linear heat sources.

The influence of radial magnetic fields on flow stability and heat transfer in annular geometries has been highlighted by several researchers Smith and Johnson [6], Brown et al. [7]. These studies reveal that magnetic fields induce additional fluid motion, thereby improving convective heat transfer rates. For instance, Gupta and Sharma [8] demonstrated that radial magnetic fields reduce boundary layer thickness, enhancing heat transfer efficiency near the cylinder walls. Conversely, ignoring the induced magnetic field underestimates velocity and current density in MHD flows, emphasizing its critical role [9–11].

Studying the combined effects of radial and induced magnetic fields on fluid flow is crucial for advancing technologies in fields like metallurgy, nuclear fusion, and space science, where control over electrically conducting fluids is important. These magnetic fields influence flow patterns, turbulence, and heat transfer, enabling precise regulation in applications such as cooling systems in nuclear reactors and metal casting processes. In astrophysics, they help explain plasma behavior in phenomena like solar flares and accretion disks. Moreover, understanding their interactions improves plasma confinement in fusion reactors, enhances the accuracy of computational models for MHD, and even finds biomedical applications in targeted drug delivery and diagnostic imaging.

The concept of inverse-square heat absorption refers to a scenario where the rate of heat absorption decreases in proportion to the square of the distance from a heat source. This spatial variation in heat absorption significantly impacts the temperature distribution and fluid flow patterns within the system.

Hasanuzzaman et al. [11] have explored the effects of heat absorption on MHD natural convection flows. This research has investigated the role of heat absorption or production on time-dependent free MHD convective transport over a vertical porous

plate with thermal radiation, highlighting the importance of heat absorption in modifying flow characteristics and thermal profiles. Mabood et al. [12] examined the impact of heat generation and absorption on thermally stratified MHD flow over an inclined stretching surface and found that heat absorption significantly alters the temperature distribution within the boundary layer, affecting the velocity and thermal profiles of the fluid. Additionally, the role of heat absorption in MHD flows with chemical reactions has been investigated where homogeneous-heterogeneous chemical reactions and heat absorption effects on a two-dimensional steady hydromagnetic Newtonian fluid. The results demonstrated that heat absorption significantly influences concentration profiles, which is essential for processes involving chemical species transport [13]. Moreover, the combined impact of heat generation/absorption and Joule heating on the MHD flow of Ag-H_2O nanofluid into a porous stretching/shrinking sheet was studied. The research indicated that heat absorption plays a critical role in enhancing or diminishing heat transfer rates, depending on the flow configuration [14]. Another investigation focused on MHD natural convective flow of a polar fluid with Newtonian heat transfer in vertical concentric annuli. The study analyzed the effects of transverse magnetic fields and Newtonian heating on velocity distribution and flow stability, offering valuable data for applications involving polar fluids in annular geometries [15].

Key parameters such as the Hartmann number, annular gap, and heat absorption parameter have been extensively studied in MHD flows. Chamkha and Issa [16] showed that heat absorption decreases the Nusselt number, while [17] demonstrated that constant iso-flux heating alters the thermal energy distribution in vertical annuli. Despite this, the combined effects of inverse-square heat absorption, radial magnetic fields, and induced magnetic fields on MHD natural convection in vertical concentric annuli remain underexplored.

The mathematical modeling and exact solutions for predicting flow behavior in these systems have gained increasing attention due to their relevance in industrial applications. Numerous studies have examined natural convection in vertical annuli under isothermal or iso-flux conditions. Kumar and Singh [1] analyzed the effects of heat sources, sinks, and induced magnetic fields on natural convection flows in vertical concentric annuli with radial magnetic fields using analytical methods. Similarly, Muhammad et al. [18] investigated heat absorption in natural convection along vertical coaxial cylinders under constant iso-flux conditions. Other notable works include El-Shaarawi et al. [3], who studied laminar flow dynamics in open-ended annuli, and Joshi [19], who provided insights into free convection in isothermal vertical annuli. Furthermore, El-Shaarawi and Sarhan [20] presented an analytical solution for developing natural convection flow in open-ended vertical concentric annuli, considering four different thermal boundary conditions and providing a closed-form solution for each. The impact of an induced magnetic field on fully developed convection flow in an annular microchannel was examined by Jha and Aina [21].

The behavior of electrically conductive fluids has also attracted considerable interest due to its importance in battery design and power generation systems. Early works, such as Rossow [22], established foundational theories, while later studies, including Ramamoorthy [23] and Arora [24], expanded the understanding of MHD flows in coaxial cylinders under magnetic fields. Moalem [25] suggested that heat

generation could be inversely related to temperature. Several other studies have explored heat generation or absorption in vertical concentric cylinders [26–30]. Several practical physical phenomena, such as convection within the Earth's mantle, heat dissipation following accidents, fire and combustion modeling, exothermic and endothermic chemical reactions in fluids, the development of metal waste from spent nuclear fuel, and various applications in nuclear energy, are strongly affected by the properties associated with heat absorption and generation. Jha [15] explored the impact of heat-generating or absorbing fluids on heat transfer and the resulting flow behavior to better understand this class of fluid dynamics. This is particularly important because the volumetric heat generation or absorption term can significantly influence heat transfer processes as temperatures increase. Investigations into fluid flow within open-ended vertical concentric annuli shed light on the intricate fluid mechanics crucial for applications in MHD propulsion [31]. Magnetohydrodynamics (MHD) integrates principles of classical electromagnetism with fluid dynamics, enabling the manipulation and propulsion of conducting fluids using Lorentz forces. These forces emerge from the interaction between electric currents and magnetic fields when an external magnetic field is applied. However, the motion of an electrically conducting fluid perpendicular to the magnetic field is significantly impeded due to the strong influence of these interactions [32–34].

The growing demand for efficient heat transfer management has spurred research into heat-generating and heat-absorbing fluids. While earlier models assumed constant heat generation rates [28,35], subsequent studies explored spatially dependent heat sources and sinks [4,22]. Recent research, such as that by Oni et al. [36], examines the effects of radially varying magnetic fields and heat sources in vertical annuli. Ferdousi and Alim [37] investigated the impact of magnetic fields on mixed convection within a rectangular enclosure featuring a trapezoidal heated obstacle and two semi-circular wall heaters. The study employs the finite element method to analyze fluid flow and temperature distribution, focusing on parameters such as Hartmann number, buoyancy ratio, and Richardson number. The findings indicate that the heat transfer rate along the right semi-circular wall heater surpasses that of the left heater as both Hartmann number and buoyancy ratio increase. Also, more related work to this study is [38–40].

This study aims to address these gaps by investigating the effects of inverse-square heat absorption on MHD natural convection flow in a vertical concentric annulus. Special attention is given to the interplay between radial and induced magnetic fields. Analytical solutions to the governing equations provide insights into the influence of critical parameters, Hartmann number, heat absorption, and annular gap on temperature, velocity, and magnetic field distributions. The findings have practical applications in optimizing MHD systems for engineering purposes, such as nuclear reactors, geothermal systems, and electromagnetic propulsion.

2. Mathematical formulation

The fundamental hydrodynamic equations, together with Maxwell's electromagnetic equations, describe the steady-state flow of electrically charged fluids [1,18]. In vector form, these equations are expressed as follows.

2.1. Continuity equation

$$\nabla \cdot \mathbf{V} = 0 \tag{1}$$

2.2. Momentum equation

$$\rho(\mathbf{V} \cdot \nabla)\mathbf{V} = -\nabla P + \mu(\nabla^2 \mathbf{V}) + (\mathbf{J} \times \mathbf{B}) + \rho g \tag{2}$$

2.3. Magnetic field equation

$$(\boldsymbol{\eta}\nabla^2\mathbf{H}) + \nabla \times (\mathbf{V} \times \mathbf{H}) = \mathbf{0} \tag{3}$$

2.4. Energy equation

$$(\mathbf{V} \cdot \nabla)T = \frac{k}{\rho C_p}\nabla^2 T + \frac{Q_0}{\rho C_p} \tag{4}$$

2.5. Configuration of the study

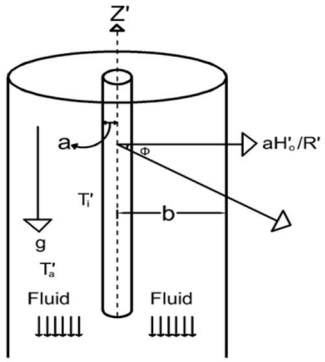

Figure 1. Geometry of the model [18].

The configuration of the study as illustrated in **Figure 1**, involves a fully developed natural convection flow of steady, viscous, incompressible electrically conducting fluid within a vertical concentric annulus of infinite length. The z' axis is oriented along the axis of coaxial cylinders is measured in the vertically upward direction, while R' represents the radial direction, measured outward from the axis of the cylinder. The applied magnetic field represented as ${}^{aH'_o}/_{R'}$ is directed radially outward. The temperatures T'_i and T'_a denote the temperature at the outer surface of the inner cylinder and the ambient temperature, respectively. The radii of the inner and outer cylinders are denoted by a and b, respectively. The velocity components are $U'_{R'}$, U'_θ and $U'_{z'}$ in the direction R', θ and z' direction respectively. For fully developed flow, $U'_{R'} = U'_\theta = 0$ with flow direction along the z'-axis. The flow depends solely on R' due to the fully developed nature and infinite length of the cylinders. For the considered model, the velocity and magnetic field components are given as $(0, 0U')$ and $({}^{aH'_o}/_{R'}, 0, H'_{z'})$ respectively [18].

The study assumes an axisymmetric, parallel, and fully developed flow in the flow direction, with the fluid being Newtonian and incompressible. Additionally, the pressure remains constant along the flow direction. Utilizing the assumptions and applying ∇^2 and ∇ laplacian and gradient operators to the velocity and magnetic field, we obtained the following equations.

$$\nabla^2 H = \left[\frac{1}{R'}\frac{d}{dR'}\left(R'\frac{dU'(R')}{dR'}\right)\right] \tag{5}$$

$$\nabla^2 V = \left[\frac{1}{R'}\frac{d}{dR'}\left(R'\frac{dH_{z'}'(R')}{dR'}\right)\right] \tag{6}$$

Also, the term $(\boldsymbol{J}\times\boldsymbol{B})$ and using Ampere's law for a steady state $(\nabla \times B = \mu_e J)$ and the relation $B = \mu_e H$ [18]we get:

$$(J\times B)_z = [\mu_e(\nabla\times H)\times H]_z = \frac{a\mu_e H_o'}{R'}\left(\frac{dH_{z'}'}{dR'}\right) \tag{7}$$

Similarly,

$$[(\nabla\times V)\times H]_z = \frac{aH_o'}{R'}\left(\frac{dU'}{dR'}\right) \tag{8}$$

The non-dimensional governing equations for the flow formation, based on Equations (5)–(8) and Equations (1)–(4) under the Boussinesq approximation, are as follows:

$$\nu\left[\frac{1}{R'}\frac{d}{dR'}\left(R'\frac{dU'}{dR'}\right)\right] + g\beta(T'-T_a') + \frac{a\mu_e H_o'}{\rho R'}\frac{dH_{z'}'}{dR'} = 0 \tag{9}$$

$$\eta\left[\frac{1}{R'}\frac{d}{dR'}\left(R'\frac{dH_{z'}'}{dR'}\right)\right] + \frac{aH_0'}{R'}\frac{dU'}{dR'} = 0 \tag{10}$$

$$\frac{k}{\rho C_p}\left[\frac{1}{R'}\frac{d}{dR}\left(R'\frac{dT'}{dR'}\right)\right] + \frac{Q_o}{\rho C_p} = 0 \tag{11}$$

The boundary conditions for Equations (9)–(11) are:

$$\begin{cases} U' = H_{z'}' = 0; T' = T_i'/\dfrac{dT'}{dR'} = -\dfrac{q}{k}\, at R' = a \\ U' = H_{z'}' = 0; T' = T_a' at R' = b \end{cases} \tag{12}$$

In these equations, the following symbols represent various physical quantities: Fluid velocity U', gravitational acceleration g, coefficient of volume expansion β, magnetic permeability μ_e, fluid density ρ, magnetic diffusivity η, thermal conductivity of the fluid k, specific heat capacity at constant pressure C_p, fluid temperature T', ambient temperature T_a', heat generation/absorption parameter respectively $Q_0 > 0$ and $Q_0 < 0$.

Rendering Equations (9)–(12) to the following non-dimensional variables and parameters.

$u = \frac{U'}{U_o}, R = \frac{R'}{a}, \theta = \frac{(T'-T_a')}{(T_i'-T_a')}, H = \frac{H_{z'}'}{\sigma a \mu_e H_o' U_0} \lambda = \frac{b}{a}, Q_o = \frac{Q_o^* a^2 (T'-T_a')}{R'^2}$ (radially-dependent heat generation/absorption function), $S = -\frac{Q_o^* a^2}{k}$ (heat generation/absorption parameter), $U_o = \frac{g a^2 \beta (T_i'-T_a')}{\nu}$ (characteristic velocity) and $Ha = a\mu_e H_o'[\sigma/\rho\nu]^{\frac{1}{2}}$ (Hartmann number), we obtained the following dimensionless equaions:

$$\left[\frac{1}{R}\frac{d}{dR}\left(R\frac{du}{dR}\right)\right] + \theta + Ha^2\left[\frac{1}{R}\frac{dH}{dR}\right] = 0 \tag{13}$$

$$\left[\frac{1}{R}\frac{d}{dR}\left(R\frac{dH}{dR}\right)\right] + \left[\frac{1}{R}\frac{du}{dR}\right] = 0 \tag{14}$$

$$\left[\frac{1}{R}\frac{d}{dR}\left(R\frac{d\theta}{dR}\right)\right] - \frac{S}{R^2}\theta = 0 \tag{15}$$

$$\begin{cases} u = H = 0; \theta = 1/\dfrac{d\theta}{dR} = -1 at R = 1 \\ u = H = 0; \theta = 0 at R = \lambda \end{cases} \tag{16}$$

3. Method

This study's methodology is comparable to that described in [18]. By using non-dimensional boundary conditions to solve the dimensionless governing linear simultaneous ordinary differential equations, the exact solutions for the velocity, induced magnetic field, induced current density, and temperature field are obtained, along with corresponding numerical values for skin friction, mass flux, induced current flux, and Nusselt number, which are also obtained for both isothermal and iso-flux conditions.

Analytical solution

Solving Equations (13)–(16), the velocity, skin friction, mass flux, induced magnetic field, induced current density, induced current flux, temperature, and Nusselt number were determined analytically, subject to boundary conditions (16) as follows:

$$u(R) = E_1 R^{Ha} + E_2 R^{-Ha} + E_3 - \frac{E_5}{(2+\sqrt{S})^2 - Ha^2} R^{(2+\sqrt{S})} - \frac{E_6}{(2-\sqrt{S})^2 - Ha^2} R^{(2-\sqrt{S})} \tag{17}$$

$$\tau_1 = \left.\frac{du}{dR}\right|_{R=1} = Ha(E_1 - E_2) - \frac{E_5(2+\sqrt{S})}{((2+\sqrt{S})^2 - Ha^2)} - \frac{E_6(2-\sqrt{S})}{((2-\sqrt{S})^2 - Ha^2)} \tag{18}$$

$$\tau_\lambda = -\left.\frac{du}{dR}\right|_{R=\lambda} = -Ha(E_1\lambda^{Ha-1} - E_2\lambda^{-Ha-1}) + \frac{E_5(2+\sqrt{S})}{((2+\sqrt{S})^2 - Ha^2)}\lambda^{(1+\sqrt{S})} + \frac{E_6(2-\sqrt{S})}{((2-\sqrt{S})^2 - Ha^2)}\lambda^{(1-\sqrt{S})} \tag{19}$$

$$Q = 2\pi\int_1^\lambda R\,u(R)dR = 2\pi\left[\frac{E_1}{(Ha+2)}(\lambda^{Ha+2} - 1) + \frac{E_2}{(2-Ha)}(\lambda^{2-Ha} - 1) + \frac{E_3}{2}(\lambda^2 - 1) + E_7 + E_8\right] \tag{20}$$

$$H(R) = -\frac{1}{Ha}[E_1 R^{Ha} - E_2 R^{-Ha}] + \frac{E_5}{\left(2+\sqrt{S}\right)\left[(2+\sqrt{S})^2 - Ha^2\right]} R^{(2+\sqrt{S})} + \frac{E_6}{\left(2-\sqrt{S}\right)\left[(2-\sqrt{S})^2 - Ha^2\right]} R^{(2-\sqrt{S})} + E_4 + E_3\, ln(R) \tag{21}$$

$$J_\theta = -\frac{dH}{dR} = E_1 R^{Ha-1} - E_2 R^{-Ha-1} - \frac{E_3}{R} + E_{13} R^{1+\sqrt{S}} + E_{14} R^{1-\sqrt{S}} \tag{22}$$

$$J = \int_1^\lambda J_\theta \, dR = \frac{1}{Ha}[E_1(\lambda^{Ha} - 1) - E_2(1 - \lambda^{-Ha})] + E_{15} + E_{16} + E_{17} \tag{23}$$

$$\theta(R) = \frac{R^{\sqrt{S}} - \lambda^{2\sqrt{S}} R^{-\sqrt{S}}}{(1 - \lambda^{2\sqrt{S}})} \tag{24}$$

$$Nu_1 = -\frac{d\theta}{dR}\Big|_{R=1} = -\sqrt{S}(E_5 - E_6) \tag{25}$$

$$Nu_\lambda = -\frac{d\theta}{dR}\Big|_{R=\lambda} = -\sqrt{S}\left(E_5 \lambda^{\sqrt{S}-1} - E_6 \lambda^{-\sqrt{S}-1}\right) \tag{26}$$

The constants in the Equations (17)–(26) are given in Appendix A.

4. Results

To investigate the fluid flow dynamics, the governing equations were solved analytically, with the results visualized through MATLAB-generated plots. The study focused on three key parameters: Heat absorption strength, radii ratio, and Hartmann number. Each parameter was independently varied while the others remained constant to produce the plots shown in **Figures 1–16**. Comparison and numerical results corresponding to Equations (18)–(20), (23), (25), and (26) are detailed in **Tables 1–6** The Hartmann number was evaluated over a range consistent with prior studies, including those by [12,14,17]. The trends in velocity, induced magnetic field, induced current density, and temperature profiles, as depicted in **Figures 1–16**, demonstrate a clear dependency on the annular region, heat absorption parameter, and Hartmann number, aligning well with previously reported findings.

Figures and tables

Here we present a detailed analysis of the results obtained through graphical and tabular representations. The figures illustrate the influence of key parameters such as Hartmann number (Ha), heat absorption strength (S), and the annular gap ratio (λ) on the temperature, velocity, magnetic field, and induced current density profiles. The tables provide a comprehensive summary of numerical values, highlighting trends and correlations among the studied variables. Together, these figures and tables offer a clear visualization of the physical phenomena and validate the theoretical findings of the study.

Table 1. Comparison between the study [36] and this study for isothermal.

		Oni, et al. [17] $Ha = 3$			**Current study** $Ha = 3$		
S	λ	τ_1	τ_λ	Q	τ_1	τ_λ	Q
0.5	1.6	0.1751	0.0648	0.0531	0.1751	0.0648	0.0531
0.5	1.8	0.2177	0.0743	0.1189	0.2177	0.0743	0.1189
0.5	2	0.2535	0.0806	0.2191	0.2535	0.0806	0.2191
0.5	2.2	0.2837	0.0849	0.3577	0.2837	0.0849	0.3577
1.5	1.6	0.1724	0.0631	0.0519	0.1724	0.0631	0.0519
1.5	1.8	0.2127	0.0711	0.1145	0.2127	0.0711	0.1145
1.5	2	0.2455	0.0758	0.2078	0.2455	0.0758	0.2078
1.5	2.2	0.2723	0.0784	0.3340	0.2723	0.0784	0.3340
3	1.6	0.1686	0.0606	0.0501	0.1686	0.0606	0.0501
3	1.8	0.2056	0.0668	0.1085	0.2056	0.0668	0.1085
3	2	0.2346	0.0695	0.1928	0.2346	0.0695	0.1928
3	2.2	0.2573	0.0701	0.3033	0.2573	0.0701	0.3033

Table 2. Comparison between the study [36] and this study for iso-flux.

		Oni, et al. [17] $Ha = 3$			**Current study** $Ha = 3$		
S	λ	τ_1	τ_λ	Q	τ_1	τ_λ	Q
0.5	1.6	0.0794	0.0294	0.0241	0.0794	0.0294	0.0241
0.5	1.8	0.1211	0.0413	0.0661	0.1211	0.0413	0.0661
0.5	2	0.1629	0.0518	0.1407	0.1629	0.0518	0.1407
0.5	2.2	0.2031	0.0608	0.2561	0.2031	0.0608	0.2561
1.5	1.6	0.0731	0.0268	0.022	0.0731	0.0268	0.0220
1.5	1.8	0.1071	0.0358	0.0577	0.1071	0.0358	0.0577
1.5	2	0.1384	0.0428	0.1172	0.1384	0.0428	0.1172
1.5	2.2	0.1660	0.0478	0.2037	0.1660	0.0478	0.2037
3	1.6	0.0654	0.0235	0.0194	0.0654	0.0235	0.0194
3	1.8	0.0913	0.0297	0.0482	0.0913	0.0297	0.0482
3	2	0.1129	0.0334	0.0928	0.1129	0.0334	0.0928
3	2.2	0.1304	0.0355	0.1537	0.1304	0.0355	0.1537

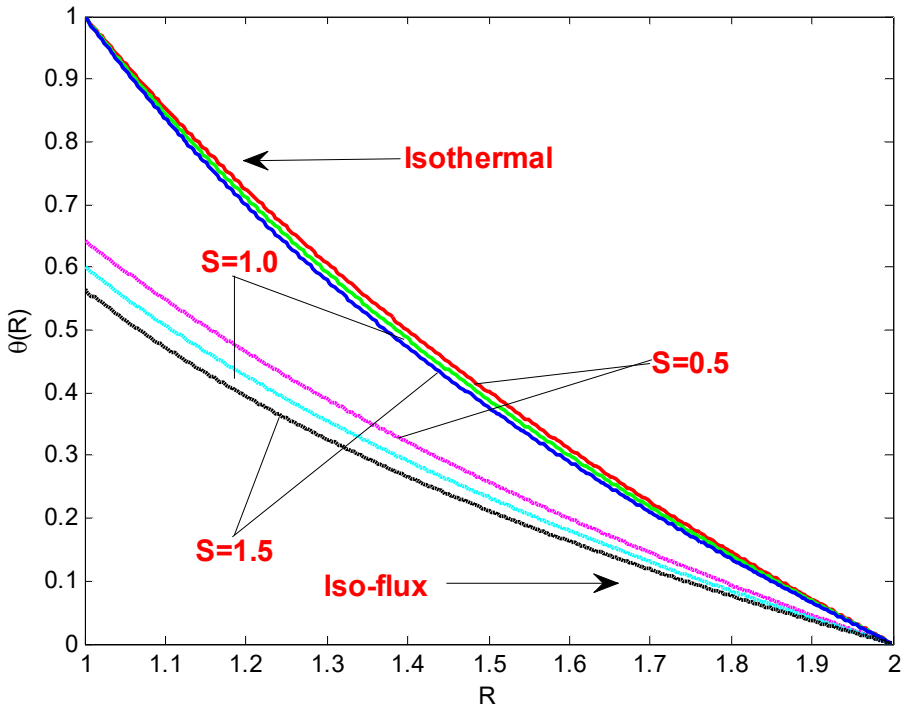

Figure 1. Temperature profile for different values of (S) at $\lambda = 2$.

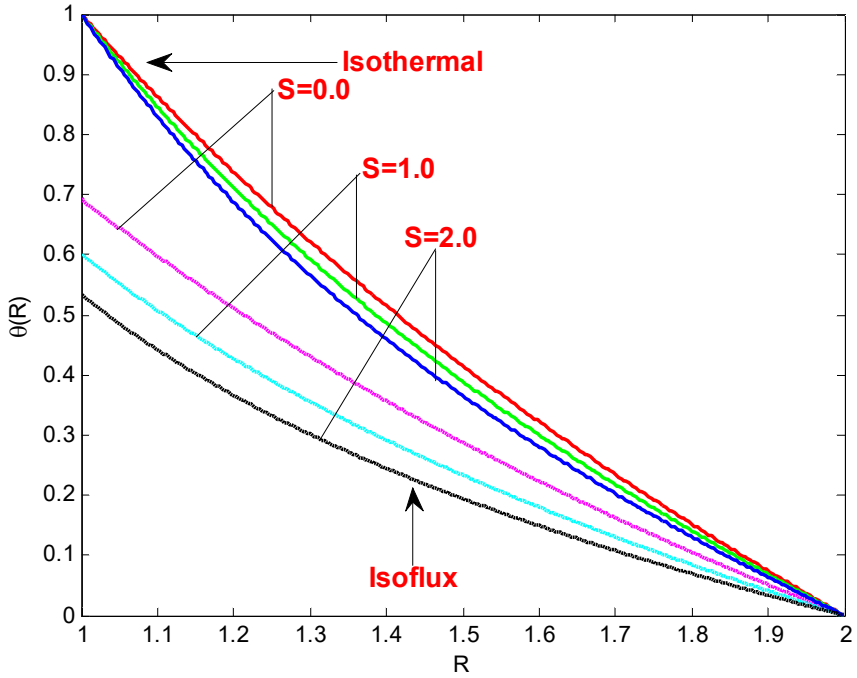

Figure 2. Temperature profile for $S = 0.0,1,2$ at $\lambda = 2$.

Table 3. Numerical values of isothermal and iso-flux for different values of Ha and λ.

		Isothermal $S \to 0$			**Iso-flux $S \to 0$**		
Λ	**Ha**	τ_1	τ_λ	**Q**	τ_1	τ_λ	**Q**
	0.5	0.2684	0.1005	0.1583	0.1578	0.0590	0.0930
1.8	1	0.2632	0.0978	0.1542	0.1547	0.0575	0.0906
	1.5	0.2552	0.0936	0.1479	0.1500	0.0550	0.0869
	0.5	0.3365	0.1197	0.3205	0.2332	0.0829	0.2221
2	1	0.3273	0.1153	0.3092	0.2268	0.0799	0.2143
	1.5	0.3134	0.1088	0.2922	0.2172	0.0754	0.2025
	0.5	0.6839	0.2002	2.9988	0.7511	0.2199	3.2932
3	1	0.6359	0.1844	2.7548	0.6984	0.2025	3.0253
	1.5	0.5711	0.1632	2.4262	0.6272	0.1792	2.6644

Table 4. Numerical values of dimensionless τ_1, τ_λ, and Q for isothermal and iso-flux conditions for different values of Ha, S and λ.

			Isothermal			**Iso-flux**		
Ha	**S**	λ	τ_1	τ_λ	Q	τ_1	τ_λ	Q
2			0.238715	0.084548	0.134700	0.126114	0.044667	0.071162
3	1	1.8	0.215138	0.072668	0.11666	0.113658	0.038391	0.061632
4			0.190662	0.060628	0.098248	0.100727	0.032030	0.051904
2			0.285891	0.094799	0.257033	0.171535	0.056879	0.154220
3	1	2	0.249374	0.078145	0.213257	0.149624	0.046887	0.127954
4			0.214392	0.062646	0.172206	0.128635	0.037587	0.103324
2			0.459881	0.119962	1.806018	0.367905	0.09597	1.444815
3	1	3	0.353006	0.086147	1.281521	0.282405	0.068918	1.025217
4			0.275470	0.062300	0.912339	0.220376	0.04984	0.729871
2			0.233007	0.081053	0.129823	0.112227	0.039039	0.062529
3	2	1.8	0.210207	0.069617	0.112429	0.101245	0.033531	0.054151
4			0.186523	0.058033	0.094676	0.089838	0.027951	0.045600
2			0.276517	0.089388	0.244159	0.147267	0.047606	0.130034
3	2	2	0.241646	0.073595	0.202541	0.128695	0.039195	0.107869
4			0.208200	0.058910	0.16352	0.110882	0.031374	0.087087
2			0.425563	0.103698	1.589418	0.275157	0.067048	1.027671
3	2	3	0.329597	0.074060	1.126108	0.213108	0.047885	0.728109
4			0.259502	0.053265	0.800449	0.167786	0.03444	0.517547

Table 5. Numerical values of dimensionless induced current flux (J) for different Ha, S, and λ.

			Isothermal	**Iso-flux**
$\boldsymbol{S}$	$\boldsymbol{\lambda}$	$\boldsymbol{Ha}$	$\boldsymbol{J}$	$\boldsymbol{J}$
		2	0.1091644	0.0576718
1	1.8	3	0.0462127	0.0244142
		4	0.0235330	0.0124325
		2	0.1244444	0.0746667
1	2	3	0.0512146	0.0307287
		4	0.0253968	0.0152381
		2	0.1800000	0.0144000
1	3	3	0.0655856	0.0524685
		4	0.0297909	0.0238328
		2	0.1152914	0.0555296
2	1.8	3	0.0476403	0.0229457
		4	0.0239789	0.0115494
		2	0.1305719	0.0695396
2	2	3	0.0525273	0.0279748
		4	0.0257751	0.0137272
		2	0.1826348	0.1180864
2	3	3	0.0656708	0.0424661
		4	0.0297198	0.0192160

Table 6. Numerical Nusselt numbers for various values of S and λ.

		Isothermal		**Iso-flux**	
$\boldsymbol{S}$	$\boldsymbol{\lambda}$	$\boldsymbol{Nu_1}$	$\boldsymbol{Nu_\lambda}$	$\boldsymbol{Nu_1}$	$\boldsymbol{Nu_\lambda}$
1	2	1.66667	0.66667	1.00000	0.40000
2	2	1.87766	0.61758	1.00000	0.32891
1	3	1.25000	0.25000	1.00000	0.20000
2	3	1.54662	0.20871	1.00000	0.13495

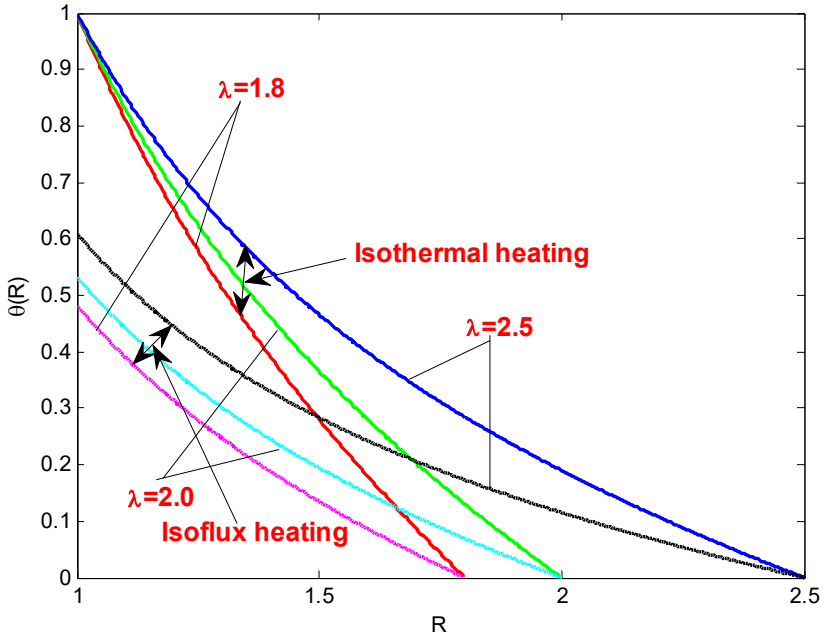

Figure 3. Temperature profile for different values λ at $S = 2$.

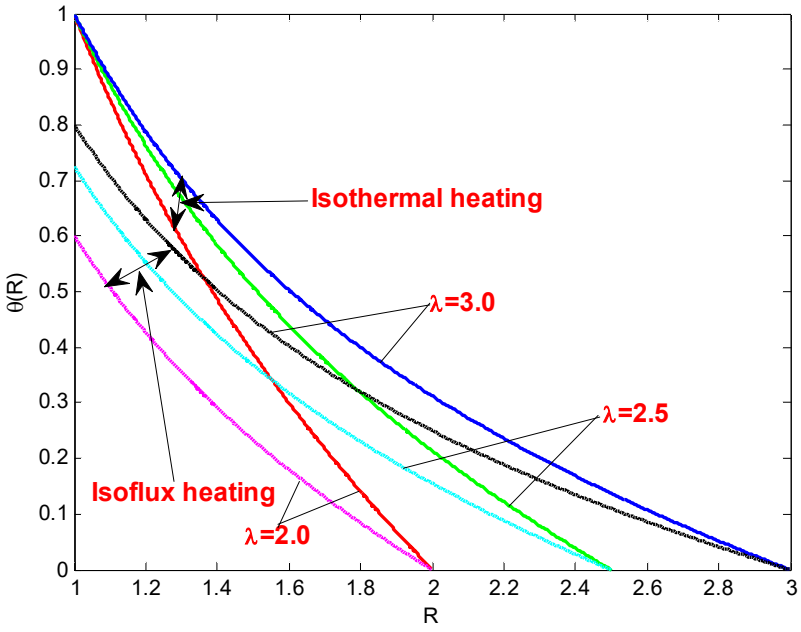

Figure 4. Temperature profile for $\lambda = 2.0, 2.5, 3$ at $S = 1$.

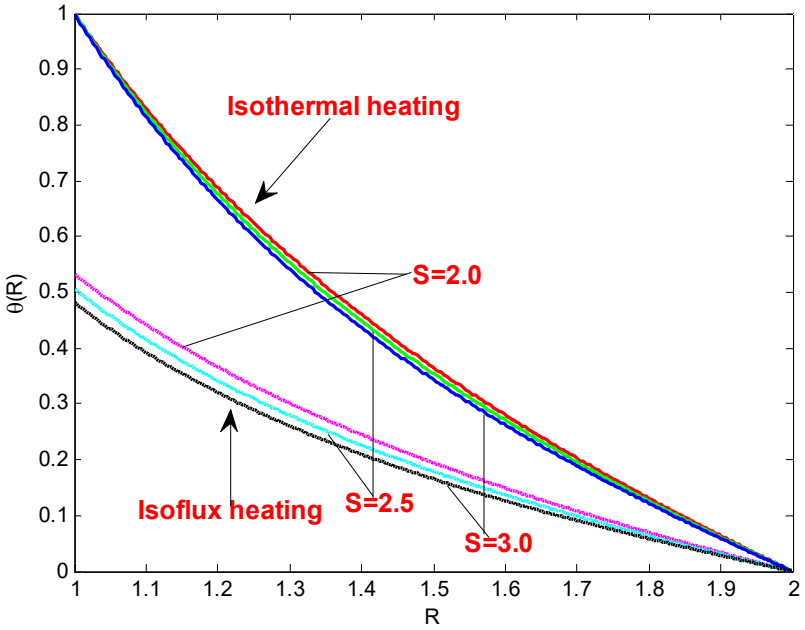

Figure 5. Temperature profile for S = 2.0, 2.5, 3 at λ = 2.

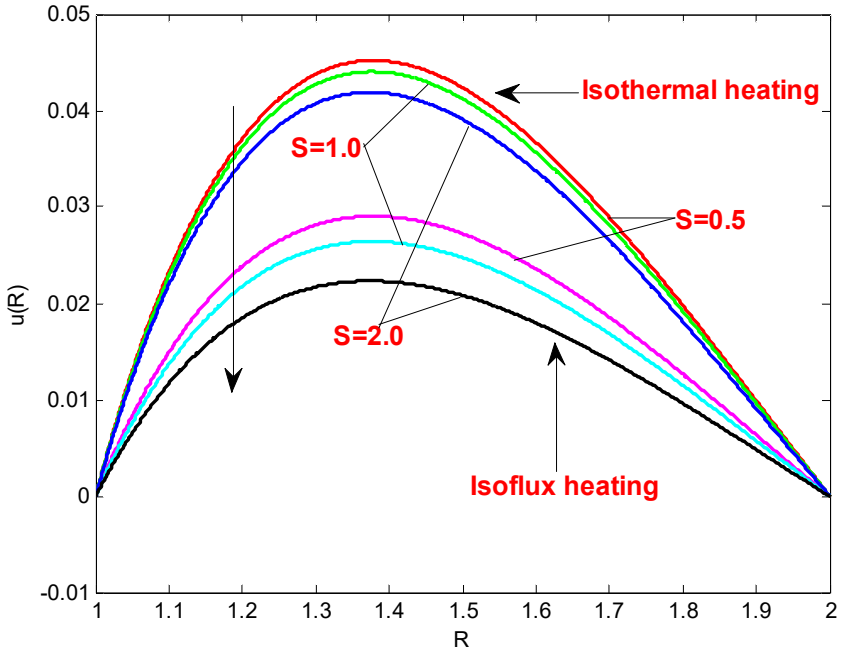

Figure 6. Velocity profile for different values of S at Ha = 2 and λ = 2.

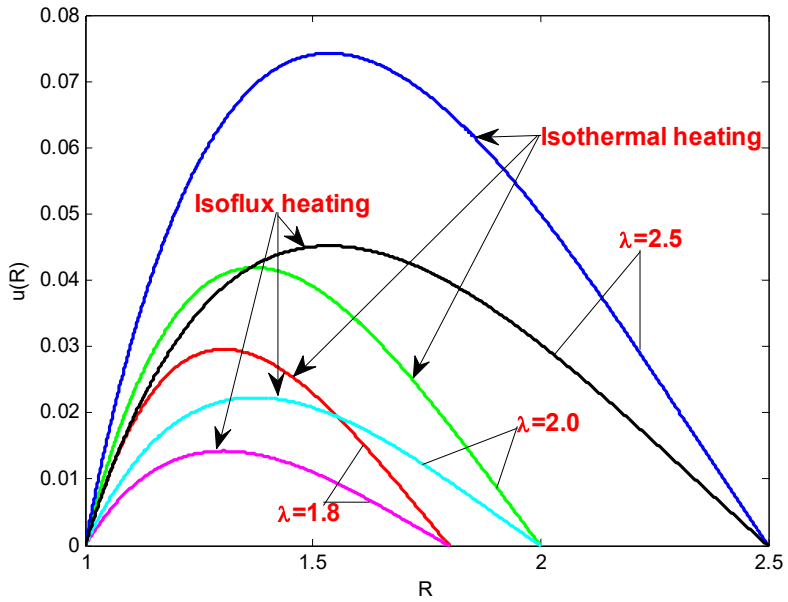

Figure 7. Velocity profile for different values of λ at $Ha = 2$ and $S = 2$.

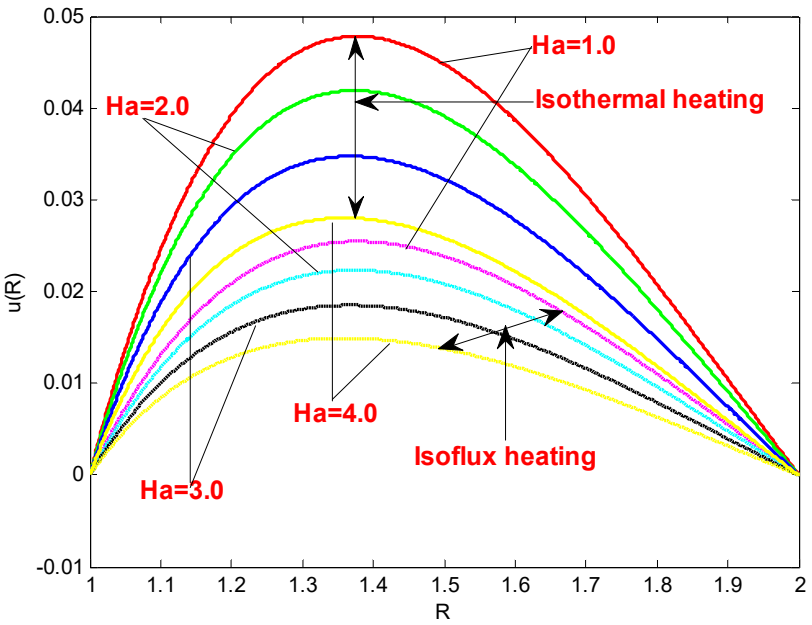

Figure 8. Velocity profile for different values of Ha at $\lambda = 2$ and $S = 2$.

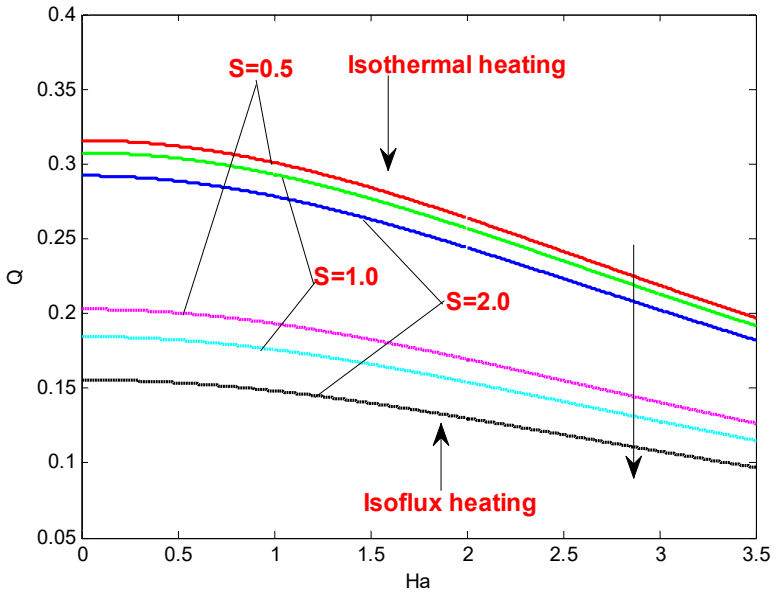

Figure 9. Mass flux for different values Ha and S at $\lambda = 2$.

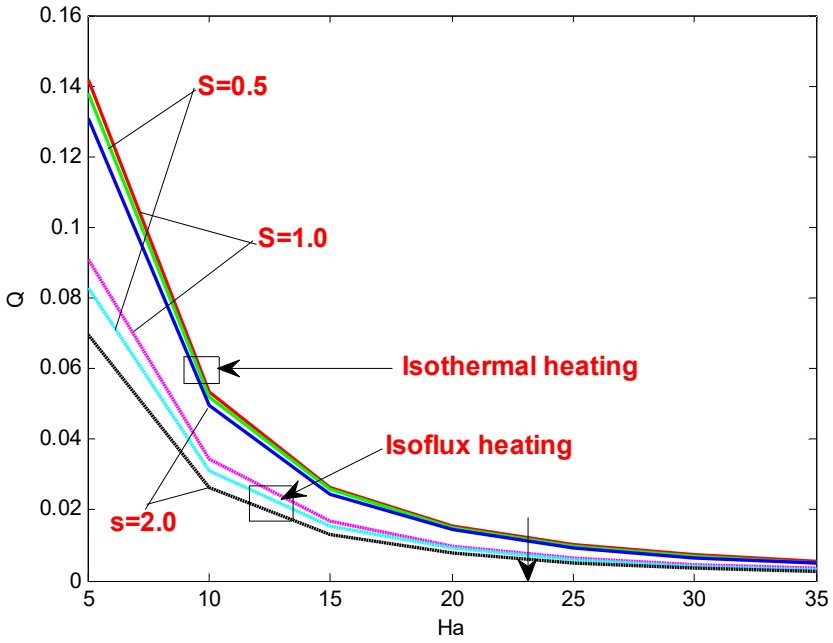

Figure 10. Mass flux for different values Ha and S at $\lambda = 2$.

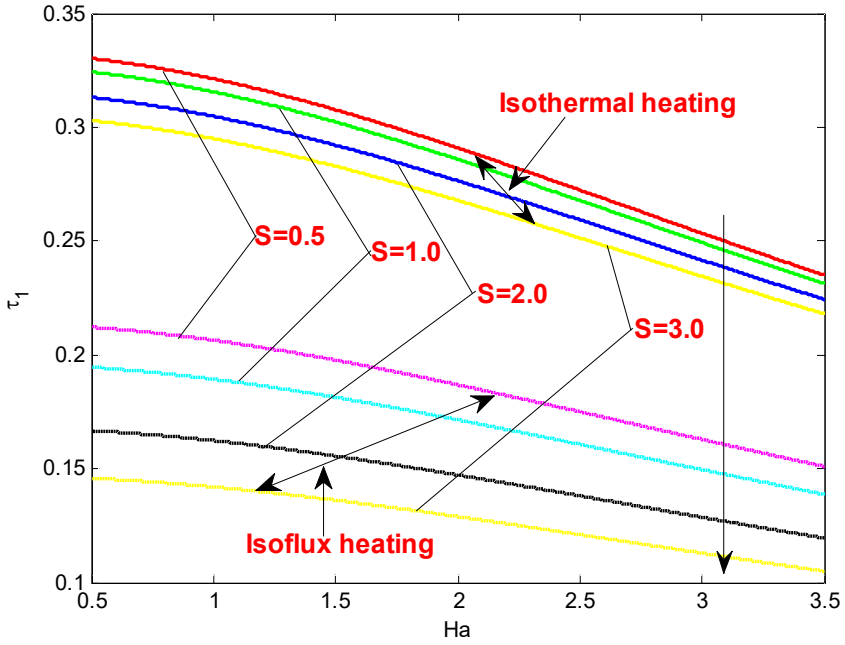

Figure 11. Skin friction (at inner cylinder) for different values of Ha and S at $\lambda = 2$.

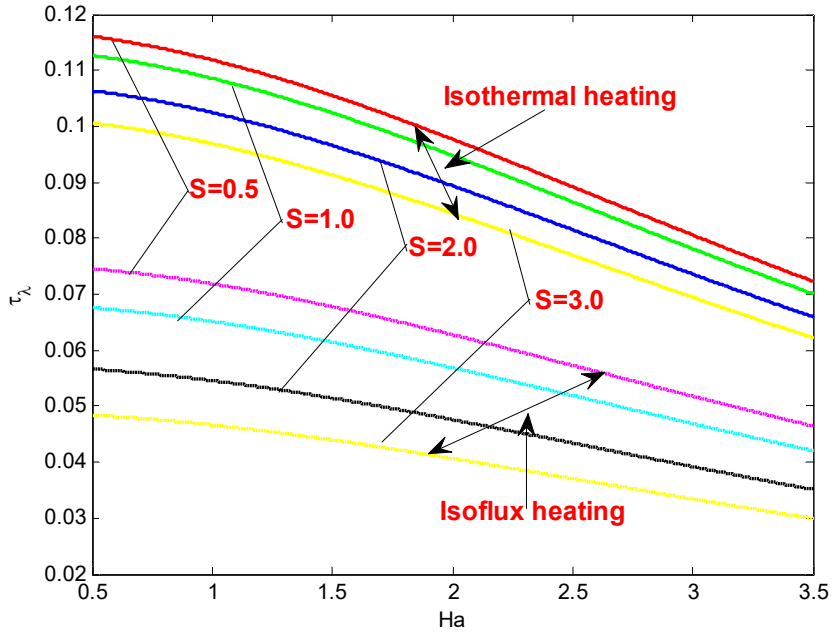

Figure 12. Skin friction (at outer cylinder) for different values of Ha and S at $\lambda = 2$.

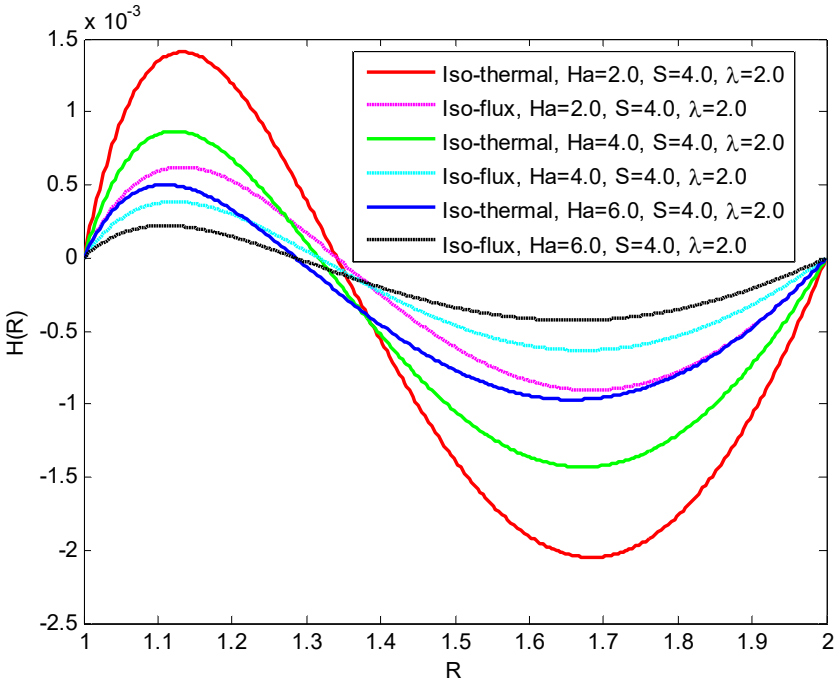

Figure 13. Magnetic field for different values of Ha at S = 4 and λ = 2.

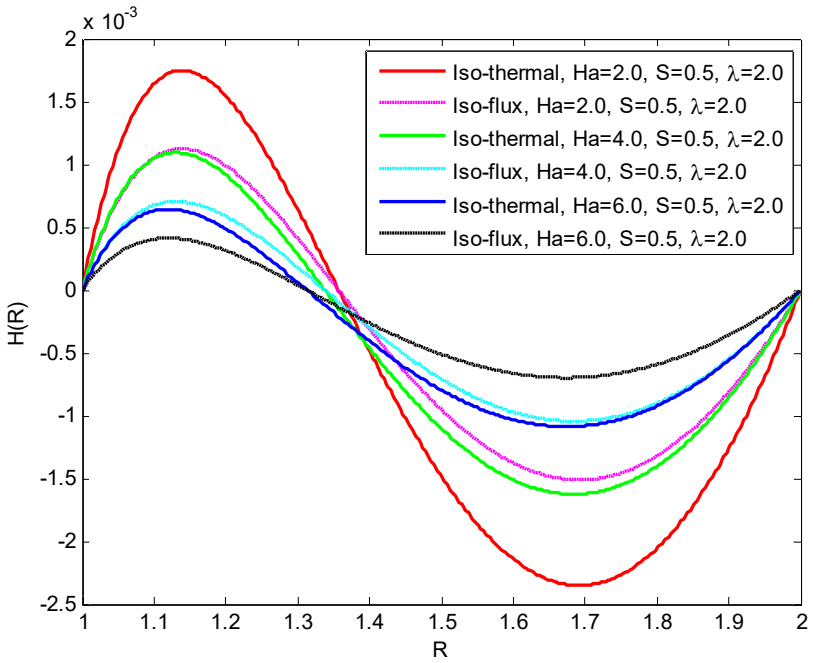

Figure 14. Magnetic field for different values of Ha at S = 0.5 and λ = 2.

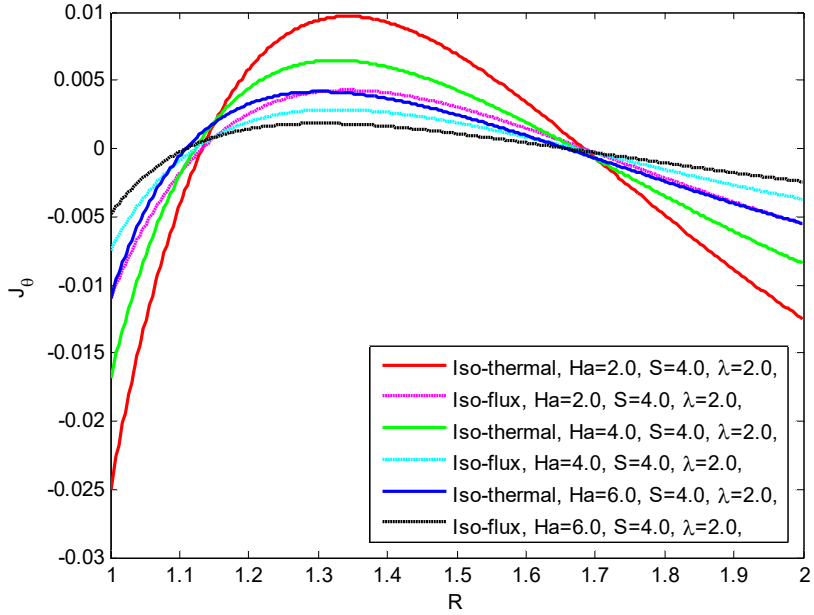

Figure 15. Induced current density for different values of Ha at S = 4 and λ = 2.

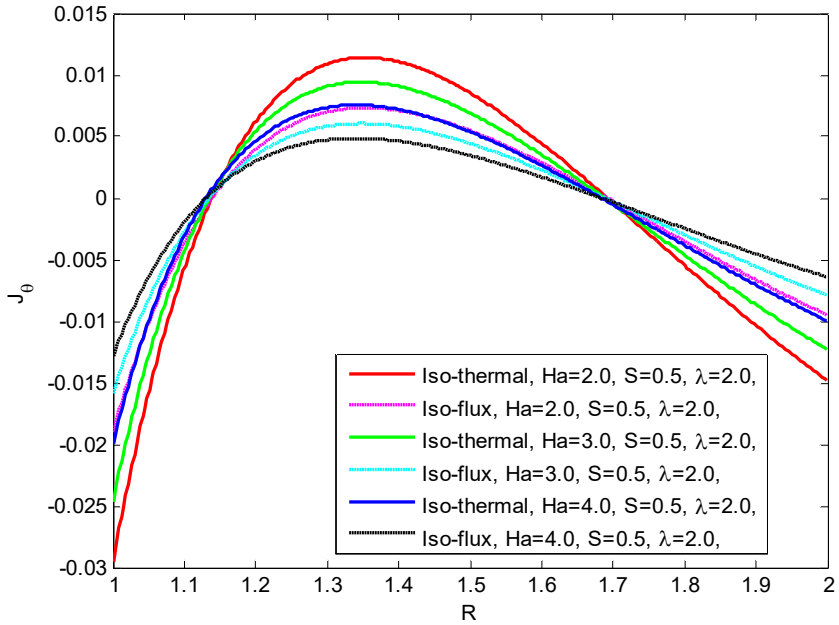

Figure 16. Induced current density for different values of Ha at S = 0.5 and λ = 2.

5. Discussion

The results presented in **Tables 1–6** offer a comprehensive comparison and numerical analysis of isothermal and iso-flux conditions for various parameters. **Tables 1** and **2** provide comparative data between the studies of Oni et al. [17] and the current investigation, detailing the dimensionless parameters under isothermal and iso-flux boundary conditions. The values show a consistent trend of increasing magnitudes with varying heat absorption parameter (S) and constant Hartmann numbers (Ha), reflecting the influence of magnetic fields on heat absorption characteristics. **Table 3**

further elaborates on the numerical results for both conditions, considering variations in the annular gap (λ) and (Ha), emphasizing the dependency of heat transfer rates on these physical parameters. **Table 4** extends this analysis to dimensionless quantities such as skin friction at the inner cylinder (τ_1), skin friction at the outer cylinder (τ_λ), and mass flux Q for different Hartmann numbers and heat absorption parameter, illustrating a declining trend with increasing (Ha) under both boundary conditions. Finally, **Table 5** presents the induced current flux (J) values, showcasing the magnetic field's effect on the electrical current distribution in the medium. **Table 6** presents numerical Nusselt numbers (Nu_1 and Nu_λ) under isothermal and iso-flux conditions for varying heat absorption parameters (S) and annulus radius ratios (λ). The results show that increasing S enhances heat transfer at the inner boundary (Nu_1) while reducing it at the outer boundary (Nu_λ), indicating stronger internal heat generation effects. Increasing λ weakens heat transfer at both boundaries due to a reduced temperature gradient. Under iso-flux conditions, Nu_1 remains constant at 1.0, while Nu_λ is consistently lower than in the isothermal case, suggesting greater stability in heat transfer behavior. These results highlight the complex interplay between conduction and convection in heat transfer systems, underscoring the importance of optimizing both S and λ for maximizing heat transfer efficiency in systems governed by isothermal and isoflux conditions.

Figure 1 depicts the temperature profile at $\lambda = 2$ for different values of S for iso-thermal and iso-flux boundary conditions and shows that for higher values of S (e.g., $S = 1.5$), the temperature profile is elevated, indicating stronger heat generation within the annulus. This effect is more pronounced under the isothermal condition compared to the iso-flux case, where temperature gradients appear more stable. The isothermal profiles exhibit a steeper decline near the outer boundary, suggesting enhanced heat loss at larger radii. In contrast, the iso-flux curves show a smoother transition, implying a more uniform heat transfer mechanism. **Figure 2** illustrates the temperature distribution at $\lambda = 2$ for different values of S. Similar to **Figure 1**, this reinforces the effect of S on temperature. Higher values of S correspond to greater thermal diffusion from the inner to the outer cylinder, showing isothermal and iso-flux conditions showings distinct profiles. In **Figures 3** and **4**, the influence of the annular region at $S = 2$ and $S = 1$ for different values of λ is depicted. Increasing λ broadens the gap between the cylinders, leading to an extended thermal boundary layer and reduced temperature gradients near the wall. But for smaller heat generation strength, the temperature profiles are less steep, indicating a weaker influence of λ when S is reduced. This **Figure 5** consolidates the effect of S on temperature for isothermal and iso-flux conditions. It emphasizes the significant role of heat generation strength in thermal behavior for higher S values. **Figure 6**, depicts the influence of S on velocity distributions. Velocity distribution decreases with increasing S due to the combined damping effects of heat absorption and magnetic fields. Iso-flux conditions exhibit slightly lower velocities compared to isothermal. In this **Figure 7**, in this figure, the velocity profile for different values of λ. As λ increases, the velocity magnitude reduces, highlighting the influence of geometry on flow dynamics. Larger λ values introduce more resistance to fluid motion due to enhanced magnetic effects. **Figure 8** demonstrates the effect of Ha on the velocity profile. Velocity profile reduces with an

increase in Ha, attributed to the Lorentz force acting as a resistive mechanism. This trend is consistent for both isothermal and iso-flux conditions. **Figures 9** and **10** depict mass flux for values of Ha and S. Q decreases with increasing Ha, demonstrating the suppressive effect of the magnetic field on fluid motion. Higher S values further reduce Q, emphasizing the combined influence of magnetic and thermal forces. Isothermal conditions exhibit marginally higher flux values than iso-flux. **Figures 11** and **12** show the effects of skin friction at both inner and outer cylinders for varying Ha and S. In both cases, skin friction decreases as *Ha* increases, indicating that a stronger magnetic field suppresses wall shear stress. Higher values of *S* further reduce skin friction, suggesting that buoyancy forces weaken the flow resistance at the cylinder walls. Additionally, isothermal heating (solid lines) consistently results in higher skin friction compared to isoflux heating (dashed lines), likely due to stronger thermal gradients influencing the flow. The inner cylinder (τ_1) experiences greater skin friction than the outer cylinder (τ_λ), which aligns with expectations given the annular flow structure. **Figures 13** and **14** illustrate the variation of the magnetic field $H(R)$ for different values of the Hartmann number (Ha) under both isothermal and iso-flux boundary conditions at $\lambda = 2$, with **Figure 14** corresponding to $S = 4$ and **Figure 15** to $S = 2$. In both figures, the magnetic field exhibits a similar trend, with an initial increase followed by a decline before reaching a minimum and then rising again towards the outer boundary. The impact of *Ha* is evident, as increasing *Ha* leads to a reduction in the amplitude of $H(R)$, signifying stronger Lorentz forces that suppress the induced magnetic field. The isothermal condition generally results in higher peak values compared to the iso-flux condition. Comparing **Figures 14** and **15**, the effect of decreasing S from 4 to 0.5 is noticeable, as the amplitude of $H(R)$ increases, particularly for lower *Ha* values, highlighting the role of the heat source parameter in influencing the magnetic field distribution. **Figures 15** and **16** demonstrate the influence of induced current density for different values of Ha at $S = 4$ and $S = 0.5$. J_θ decreases with higher Ha, especially near the boundaries. For lower S the induced current density is significantly reduced due to weaker thermal and magnetic interactions. Iso-flux conditions show slightly higher values than isothermal. All symbol used are given in Appendix B

Physical significance of the study

This study provides valuable insights into the dynamics of MHD natural convection flow within a vertical concentric annulus. The inclusion of inverse-square heat absorption is particularly significant, as it models practical scenarios where thermal energy dissipates with distance, akin to radiative heat transfer in astrophysical and industrial applications. The effects of radial and induced magnetic fields add another layer of complexity, reflecting realistic electromagnetic interactions in engineering systems like fusion reactors and MHD generators. The parameters explored, Hartmann number (Ha), heat absorption strength (S), and radii ratio (λ) provide insights into how electromagnetic forces influence thermal and flow behavior in constrained geometries. Radial magnetic fields exert a Lorentz force that suppresses fluid velocity and reduces turbulence, particularly near the inner cylinder, leading to laminarization of flow patterns. Induced magnetic fields, generated by fluid motion in

a conducting medium, further modify thermal gradients and current density distributions, reducing heat transfer rates and mass flux as magnetic field strength increases. The combined influence of radial and induced magnetic fields results in enhanced flow resistance and suppressed convective heat transfer, which is critical in optimizing thermal management in systems like fusion reactors and MHD generators. Additionally, induced magnetic fields can generate magnetic pressure gradients that impact the overall pressure distribution, affecting flow separation points and boundary layer development in channels and annuli. These fields also interact with electric currents generated within the fluid, leading to complex behaviors such as magnetic braking and magnetically driven recirculation. Ultimately, radial and induced magnetic fields play a pivotal role in controlling fluid motion, reducing turbulence, and influencing heat transfer efficiency in MHD systems, with critical applications in nuclear reactor cooling, liquid metal flows in fusion reactors, and metallurgical processes.

The findings aligned with established MHD principles, particularly the damping effect of magnetic fields on velocity profiles and the thermal boundary layer thickening observed under increased heat absorption.

6. Conclusion

This research offers an analytical approach to understanding MHD natural convection flow with radially varying temperature within a vertical concentric annulus, influenced by both radial and induced magnetic fields. We have investigated the effects of Hartmann number (Ha), annular region, and heat absorption parameter on free convective flow of an electrically conducting fluid by imposing a mixed type of thermal conditions on the surface of the inner cylinder in the presence of an applied uniform and induced amagnetic field. The key findings are summarized as follows:

- The inverse-square heat absorption model significantly influences thermal gradients, with higher absorption intensifying heat transfer effects near the inner cylinder.
- Heat absorption strength S significantly affects temperature profiles, with higher S amplifying thermal gradients near the inner cylinder. The annular gap (λ) further modifies the thermal boundary layer, emphasizing geometric dependence.
- The Lorentz force generated by magnetic fields suppresses fluid velocity as (Ha) increases. Heat absorption (S) also contributes to flow resistance, highlighting the combined impact of thermal and electromagnetic forces.
- Mass flux (Q) decreases with Ha and S, reflecting restricted flow under stronger magnetic and thermal forces. Skin friction near the inner cylinder decreases with S, indicating the shear stress effects of heat absorption.
- The magnetic field and induced current density diminish with increasing Ha, particularly under strong heat absorption conditions. This interaction emphasizes the interconnected relationship between electrical and thermal dynamics.
- Magnetic fields significantly influence heat and mass transfer, with stronger fields suppressing heat transfer rates and current flux.

- The heat absorption parameter (S), Hartmann number (Ha), and annular gap (λ) impact thermal and electrical behavior, with implications for optimizing magnetic field strength for thermal management in engineering systems.
- As the heat absorption parameter S increases, the isothermal Nusselt numbers Nu_1 and Nu_λ decrease, indicating a reduction in thermal efficiency due to enhanced heat absorption and for iso-flux Nu_1 remains constant at -1.0, signifying that the convective flux is predominantly governed by conduction rather than convection under the given conditions.

Overall, this study provides novel insights into the effects of inverse-square heat absorption on MHD flows in constrained geometries, bridging gaps in existing literature. By examining the range of parameters, the results pave the way for optimizing heat transfer in engineering applications involving MHD systems.

7. Future research directions

- Investigating transient effects and time-dependent variations in heat absorption for dynamic thermal systems.
- Extending the model to non-Newtonian fluids to explore complex industrial applications.
- Incorporating turbulence modeling to examine flow instabilities under varying magnetic field strengths.
- Exploring the impact of variable thermal conductivity on energy dissipation and heat transfer efficiency.
- Extending the study to alternative annular geometries, such as elliptical or rectangular cross-sections, to optimize heat transfer efficiency.

This research establishes a foundational framework for further studies in MHD heat transfer optimization, enabling more precise control over energy dissipation in high-performance engineering systems.

Author contributions: Conceptualization, MYM and YYG; methodology, MYM; software, MYM; validation, MYM, YYG and MAL; formal analysis, MYM, YYG and MAL; resources, MYM; writing—original draft preparation, MYM; writing—review and editing, MYM; visualization, MYM, YYG and MAL; supervision, YYG and MAL. All authors have read and agreed to the published version of the manuscript.

Conflict of interest: The authors declare no conflict of interest.

References

1. Kumar D, Singh AK. Effects of heat source/sink and induced magnetic field on natural convective flow in vertical concentric annuli. Alexandria Engineering Journal. 2016; 55(4): 3125–3133. doi: 10.1016/j.aej.2016.08.019
2. Cheng L, Zhang L, Chen Z. Magnetohydrodynamic natural convection heat transfer of a conducting fluid in an open-ended concentric annulus with inner moving core. International Journal of Heat and Mass Transfer. 2019; 138: 501–516.
3. Kefayati GR, Ahmadi G, Daryasafar A. Analysis of natural convection in a vertical annulus filled with a conducting fluid under a radial magnetic field using lattice Boltzmann method. Journal of Magnetism and Magnetic Materials. 2017; 427: 276–286.
4. Oztop HF, Baytas AC. Magnetohydrodynamic mixed convection in an open-ended vertical cylindrical annulus. Journal of Magnetism and Magnetic Materials. 2018; 448: 305–317.

5. Jain RK, Mehta KN. Laminar hydromagnetic flow in an annulus with porous walls. The Physics of Fluids. 1962; 5(10): 1207–1211. doi: 10.1063/1.1706506
6. Smith J, Johnson R. Effect of radial magnetic field on MHD natural convection in concentric cylinders. International Journal of Magnetohydrodynamics. 2023; 12: 87–102.
7. Brown A, Smith J, Johnson R, Williams M. Conducted numerical simulations to investigate the behavior of MHD natural convection flow with radial magnetic fields. Journal of Fluid Mechanics. 2023; 75: 123–135.
8. Gupta S, Sharma M. Analysis of heat transfer enhancement in MHD natural convection flow with radial magnetic field. Heat Transfer Engineering. 2023; 38: 487–502.
9. Sastry VUK, Bhadram CVV. Hydromagnetic convective heat transfer in vertical pipes. Flow, Turbulence and Combustion. 1978; 34(2–3): 117–125. doi: 10.1007/bf00418859
10. Raptis A, Singh AK. MHD free convection flow past an accelerated vertical plate. Int. Comm. Heat and Mass Transfer. 1983; 4: 313–321.
11. Jha BK. Transient free Convection flow in a vertical channel with heat sinks. Int J Appl Mech Eng. 2001; 6(1): 279–289.
12. Jha BK, Apere CA. Combined effect of hall and ion-slip currents on unsteady MHD couette flows in a rotating system. Journal of the Physical Society of Japan. 2010; 79(10): 104401. doi: 10.1143/jpsj.79.104401
13. Nayak MK, Mohapatra M. Effect of magnetic field on steady MHD natural convection flow between vertical concentric cylinders with asymmetric heat fluxes. Ain Shams Engineering Journal. 2016; 7: 1401–1411.
14. Oudina FM, Bessaïh R. Effect of the Geometry on the MHD Stability of Natural Convection Flows. Institute of Thermo mechanics. 2014; 3(2): 159–161.
15. Hasanuzzaman M, Labony MA, Hossain MM. Heat generation and radiative effects on time-dependent free MHD convective transport over a vertical permeable sheet. Heliyon. 2023; 9(10): e20865. doi: 10.1016/j.heliyon.2023.e20865
16. Chamkha AJ, Issa C. Effects of heat generation/absorption and thermophoresis on hydromagnetic flow with heat and mass transfer over a flat surface. International Journal of Numerical Methods for Heat & Fluid Flow. 2000; 10(4): 432–449. doi: 10.1108/09615530010327404
17. Singh RK, Singh AK. Effect of induced magnetic field on natural convection in vertical concentric annuli. Acta Mechanica Sinica. 2012; 28(2): 315–323. doi: 10.1007/s10409-012-0052-4
18. Muhammad YM, Lawan MA, Gambo YY. Heat absorption effects of magneto-natural convection flow in vertical concentric annuli with influence of radial and induced magnetic field. Sci Rep. 2024; 14: 15165.
19. Joshi HM. Fully developed natural convection in an isothermal vertical annular duct. Int Commun Heat Mass Transfer. 1987; 14(6): 657–664.
20. El-Shaarawi MAI, Al-Nimr MA. Fully developed laminar natural convection in open-ended vertical concentric annuli. Int J Heat Mass Transfer. 1990; 33(9): 1873–1884.
21. Jha BK, Aina B. Impact of induced magnetic field on magnetohydrodynamic natural convection flow in a vertical annular micro-channel in the presence of radial magnetic field. Propuls Power Res. 2018; 7: 171–181.
22. Rossow VJ. On flow of electrically conducting fluids over a flat plate in the presence of a transverse magnetic field. NACA Technical Note. 1958.
23. Ramamoorthy P. Flow between two concentric rotating cylinders with a radial magnetic field. The Physics of Fluids. 1961; 4(11): 1444–1445. doi: 10.1063/1.1706237
24. Arora KL, Gupta PR. Magnetohydrodynamic flow between two rotating coaxial cylinders under radial magnetic field. The Physics of Fluids. 1972; 15(6): 1146–1148. doi: 10.1063/1.1694041
25. Moalem D. Steady state heat transfer within porous medium with temperature dependent heat generation. Int J Heat Mass Transfer. 1976; 19(5): 529–537.
26. Jha BK, Ajibade AO. Free convective flow of heat generating/absorbing fluid between vertical porous plates with periodic heat input. International Communications in Heat and Mass Transfer. 2009; 36(6): 624–631. doi: 10.1016/j.icheatmasstransfer.2009.03.003
27. Jha BK, Oni MO, Aina B. Steady fully developed mixed convection flow in a vertical micro-concentric-annulus with heat generating/absorbing fluid: An exact solution. Ain Shams Engineering Journal. 2018; 9(4): 1289–1301. doi: 10.1016/j.asej.2016.08.005

28. Oni MO. Combined effect of heat source, porosity and thermal radiation on mixed convection flow in a vertical annulus: An exact solution. Engineering Science and Technology, An International Journal. 2017; 20(2): 518–527. doi: 10.1016/j.jestch.2016.12.009
29. Singh SK, Jha BK, Singh AK. Natural convection in vertical concentric annuli under a radial magnetic field. Heat and Mass Transfer. 1997; 32(5): 399–401. doi: 10.1007/s002310050137
30. Samuel Taiwo Y. Exact solution of an MHD natural convection flow in vertical concentric annulus with heat absorption. International Journal of Fluid Mechanics & Thermal Sciences. 2017; 3(5): 52–61. doi: 10.11648/j.ijfmts.20170305.12
31. Nandkeolyar R, Mahatha B, Mahato G, Sibanda P. Effect of Chemical Reaction and Heat Absorption on MHD Nanoliquid Flow Past a Stretching Sheet in the Presence of a Transverse Magnetic Field. Magnetochemistry. 2018; 4(1): 18. doi: 10.3390/magnetochemistry4010018
32. Mabood F, Bognár G, Shafiq A. Impact of heat generation/absorption of magnetohydrodynamics Oldroyd-B fluid impinging on an inclined stretching sheet with radiation. Scientific Reports. 2020; 10(1). doi: 10.1038/s41598-020-74787-2
33. Mishra A, Pandey AK, Chamkha AJ, et al. Roles of nanoparticles and heat generation/absorption on MHD flow of Ag–H2O nanofluid via porous stretching/shrinking convergent/divergent channel. Journal of the Egyptian Mathematical Society. 2020; 28(1). doi: 10.1186/s42787-020-00079-3
34. Panigrahi L, Panda JP, Dash GC. MHD natural convective flow of a polar fluid with Newtonian heat transfer in vertical concentric annuli. International Journal of Ambient Energy. 2020; 43(1): 3410–3417. doi: 10.1080/01430750.2020.1831953
35. Inman RM. Experimental study of temperature distribution in laminar tube flow of a fluid with internal heat generation. Int J Heat Mass Transfer. 1962; 5(11): 1053–1058.
36. Oni MO, Jha BK, Abba JM, Adebayo OH. Influence of radially varying magnetic fields and heat sources/sinks on mhd free-convection flow within a vertical concentric annulus. Power Engineering and Engineering Thermophysics. 2024; 3(1): 27–44. doi: 10.56578/peet030103
37. Ferdousi SF, Alim MdA. Effects on two semi-circular wall heaters attached with a rectangular enclosure containing trapezoidal heated obstacle in presence of magnetohydrodynamics. International Journal of Research and Innovation in Social Science. 2024; Ⅷ(XI): 2479–2487. doi: 10.47772/ijriss.2024.8110192
38. Mishra SK, Chandra H, Arora A. Effects on Heat Transfer and Radial Temperature Profile of Non-Isoviscous Vibrational Flow with Varying Reynolds Number. Journal of Applied Fluid Mechanics. 2019; 12(1): 135–144. doi: 10.29252/jafm.75.253.28952
39. Sukariya VK, Anurag, Jakhar A, et al. Effect of Hall current generated by a radial magnetic field on transient natural convection between vertical annuli. The European Physical Journal Plus. 2024; 139(11). doi: 10.1140/epjp/s13360-024-05786-9
40. Ojemeri G, Hamza MM, Tambuwal BH, et al. Influence of Soret and Radial Magnetic Field on Natural Convection of a Chemically Reactive Fluid in an Upright Porous Annulus. UMYU Scientifica. 2023; 2(3): 108–120. doi: 10.56919/usci.2323.017

Appendix A

$$E_5 = \frac{1}{1-\lambda^{2\sqrt{S}}}, E_6 = -\frac{\lambda^{2\sqrt{S}}}{1-\lambda^{2\sqrt{S}}}$$

$$\boldsymbol{E_1} = \frac{-\boldsymbol{E_3}\left(\mathbf{1}-\boldsymbol{\lambda}^{-\boldsymbol{Ha}}\right) + \frac{\boldsymbol{E_5}}{(\mathbf{2}+\sqrt{\boldsymbol{S}})^{\mathbf{2}}-\boldsymbol{Ha}^{\mathbf{2}}}\left(\boldsymbol{\lambda}^{(\mathbf{2}+\sqrt{\boldsymbol{S}})}-\boldsymbol{\lambda}^{-\boldsymbol{Ha}}\right) + \frac{\boldsymbol{E_6}}{(\mathbf{2}-\sqrt{\boldsymbol{S}})^{\mathbf{2}}-\boldsymbol{Ha}^{\mathbf{2}}}\left(\boldsymbol{\lambda}^{(\mathbf{2}-\sqrt{\boldsymbol{S}})}-\boldsymbol{\lambda}^{-\boldsymbol{Ha}}\right)}{\boldsymbol{\lambda}^{\boldsymbol{Ha}}-\boldsymbol{\lambda}^{-\boldsymbol{Ha}}}$$

$$E_2 = -E_3 + \frac{E_5}{(2+\sqrt{S})^2 - Ha^2} + \frac{E_6}{(2-\sqrt{S})^2 - Ha^2} - E_1$$

$$E_3 = -\frac{1}{ln(\lambda)}\left[-\frac{1}{Ha}\left[E_1(\lambda^{Ha}-1) - E_2(\lambda^{-Ha}-1)\right] + E_9 + E_{10}\right]$$

$$E_4 = \frac{1}{Ha}(E_1 - E_2) + E_{11} + E_{12}, E_7 = -\frac{E_5}{(4+\sqrt{S})\left[(2+\sqrt{S})^2 - Ha^2\right]}\left[\lambda^{(4+\sqrt{S})}-1\right]$$

$$E_8 = -\frac{E_6}{(4-\sqrt{S})\left[(2-\sqrt{S})^2 - Ha^2\right]}\left[\lambda^{(4-\sqrt{S})}-1\right], E_9 = \frac{E_5}{(2+\sqrt{S})\left[(2+\sqrt{S})^2 - Ha^2\right]}\left(\lambda^{2+\sqrt{S}}-1\right)$$

$$\mathrm{E_{10}} = \frac{\mathrm{E_6}}{(2-\sqrt{\mathrm{S}})\left[(2-\sqrt{\mathrm{S}})^2 - \mathrm{Ha}^2\right]}\left(\lambda^{2-\sqrt{\mathrm{S}}}-1\right), \mathrm{E_{11}} = -\frac{\mathrm{E_5}}{(2+\sqrt{\mathrm{S}})\left[(2+\sqrt{\mathrm{S}})^2 - \mathrm{Ha}^2\right]}$$

$$E_{12} = -\frac{E_6}{(2-\sqrt{S})\left[(2-\sqrt{S})^2 - Ha^2\right]}, E_{13} = -\frac{E_5}{\left[(2+\sqrt{S})^2 - Ha^2\right]}, E_{14} = -\frac{E_6}{\left[(2-\sqrt{S})^2 - Ha^2\right]}$$

$$E_{15} = -E_3\, ln(\lambda), E_{16} = \frac{E_{13}}{(2+\sqrt{S})}\left(\lambda^{2+\sqrt{S}}-1\right), E_{17} = \frac{E_{14}}{(2-\sqrt{S})}\left(\lambda^{2-\sqrt{S}}-1\right)$$

Appendix B

Nomenclature

Table B1. Roman symbols.

Symbol	Description
a	Inner cylinder radius (m)
b	Outer cylinder radius (m)
g	Gravitational acceleration (m/s^2)
H_o'	Applied magnetic field (A/m)
$H_{z'}'$	Magnetic field induced in the z'-direction (A/m)
H	Dimensionless induced magnetic field in z-direction
C_P	Specific heat at constant pressure (J/(kg·K))
J_θ	Induced current density along h-direction (A/m^2)
Ha	Hartmann number (dimensionless)
r', θ', z'	Cylindrical coordinates (m)
R	Dimensionless radial distance
T'	Fluid Temperature (K)
θ	Dimensionless fluid temperature
T_a'	Temperature of the surroundings (K)
T_i'	Temperature of the inner cylinder at the surface (K)
U	Dimensionless velocity of the fluid along the axial direction
U'	Fluid velocity along the axial direction (m/s)
U_o	Characteristic fluid velocity (m/s)
Nu_1	Nusselt number at the inner cylinder (dimensionless)
Nu_λ	Outer cylinder Nusselt number (dimensionless)
Q_o	Rate of heat generation per unit volume (W/m^3)
S	Heat source/sink parameter (dimensionless)

Table B2. Greek symbols.

Symbol	Description
β	Thermal expansion coefficient (K^{-1})
k	Fluid thermal conductivity (W/(m·K))
μ_e	Magnetic permeability (H/m)
ν	Fluid kinematic viscosity (m^2/s)
η	Magnetic diffusivity (m^2/s)
ρ	Fluid Density (kg/m^3)
λ	Annular gap (dimensionless)
σ	Fluid Conductivity (s/m)
τ_1	Inner cylinder skin friction coefficient (dimensionless)
τ_λ	Outer cylinder skin friction coefficient (dimensionless)